strain
An International Journal for Experimental Mechanics

Interpretation of Fringes Produced by Time-Averaged Projection Moiré

M. Ragulskis* and Z. Navickas†

*Research Group for Mathematical and Numerical Analysis of Dynamical Systems, Kaunas University of Technology, Kaunas, Lithuania
†Department of Applied Mathematics, Kaunas University of Technology, Kaunas, Lithuania

ABSTRACT: New exact formulas describing the observed shift of projected moiré grating lines on a surface of an object are derived for the paraxial model. These formulas enable to construct more accurate explicit relationship among the amplitude of oscillation, the pitch of the projected grating and the order of the fringe. Analytical derivations and numerical illustrations are used throughout the text to explain the process of formation of double-exposure and time-averaged projection moiré fringes.

KEY WORDS: *Bessel functions, projection moiré, time-averaged fringes*

1. Introduction

The projection moiré technique which belongs to the family of structured light projection methods allows obtaining the relief of an object [1–3]. Its principle consists of projecting a sinusoidal grating of parallel lines onto the surface of the object. The relief then can be deduced from the geometric parameters of the set-up and the analysis of the grating observed by a digital camera.

Another classical application of the projection moiré method is the measurement of out-of-plane displacements by the difference in relief between two prompting states. Images of projected gratings are captured on the test object before and after the object is deformed. The displacement field can be extracted from the fringe pattern produced by double exposure of these two images of the projected grid. A drawback of projection moiré techniques is associated with the projection-oriented nature of this method. Applications with non-viewable, hidden or inaccessible surfaces exclude the use of projection moiré [4].

Although classical, projection moiré techniques are continuously developed. Recently, two wavelengths of the projection topography and the synchronisation between a CCD camera and the projector were used to treat large-step discontinuities in 3D measured objects [5]. Phase-shifting fringe analysis is used to enhance the measurement resolution of the grating projection moiré topography [6]. Fast Fourier Transform and signal-demodulating techniques can be used to generate a wrapped phase map from a pattern of projection moiré fringes [7]. An unwrapping procedure is used to obtain a continuous phase; a digital method for fractional fringe multiplication helps to increase the accuracy of the method. Computer-aided moiré methods use the versatility of modern computers not only for practical measurements but also for teaching moiré techniques [8].

Applicability of projection moiré techniques for dynamical systems has been noted several decades ago. A fixed moiré grating is projected on a surface of a liquid. The wave-carrying surface distorts the grating and permits visualisation and measurement of waves as they travel across the surface [9]. Projection moiré was found useful to measure vibration of plates and other objects [10, 11].

Novel and modern applications of projection moiré are developed continuously. Projection moiré is probably one of the best experimental methods for measuring instantaneous out-of-plane deflections of composite plates on the leading edges of wings subject to bird strikes [12]. A combination of object-adapted fringes and moiré-filtering is used to monitor the exact position of a rotating fan with seven wings rotating with 100 Hz and to detect a shape defect of a single wing with 500 measurements per second [13]. Projection moiré techniques are successfully used in biomedical applications for analysis of muscular functionality [14].

Nevertheless, interpretation of projected moiré fringes is not a straightforward task even for a static double-exposure problem. This problem is poorly conditioned because of the usual difficulty of determining accurately small changes in a large quantity [15]. Nevertheless, approximate formulas for the

doi: 10.1111/j.1475-1305.2009.00625.x

interpretation of projection moiré fringes exist even for complex geometrical set-ups [16]. A CCD camera calibration procedure and improved phase extraction procedures using a modified Hilbert transform with Laplacian pyramid algorithms help to minimise the uncertainty of the measurements [17]. The inverse problem of fringe interpretation can also be solved by the help of optimisation techniques when a residual functional is built by summing over differences between displacements measured experimentally by projection moiré and those predicted numerically. Its minimisation yields a correct field of displacements of a hyper-elastic membrane [18].

Interpretation of experimental results becomes even more complicated when time-averaging projection moiré techniques are used to generate a pattern of time-averaged fringes on an oscillating surface. Quantitative analysis of the resultant time-averaged fringes has been performed with the help of equations developed by time-averaging the optical intensity of the projected grid throughout the vibrational period of the test item surface [19]. Unfortunately, authors have used a rather naïve approach for the analysis of time-averaging processes [19] – they discuss about 'splitting' of time-averaged fringes instead of manipulating with analytical relationships governing the physical processes of fringe formation. An alternative approach is presented in reference [20] where a series of precisely timed digital images of a vibrating object is recorded instead of capturing a time-averaged image.

This paper has two objectives: the first one was to derive an exact relationship describing the formation of the projected image on a deformed surface without any simplifications related to the variation of that surface; the second one was to exploit this relationship for the investigation of time-averaged images on an oscillating surface.

2. Basic Formulations

Initially, we concentrate on a one-dimensional problem (Figure 1). A structured light (usually a harmonic grating) is projected on a deformed diffuse white surface $G(x)$; the angle of illumination is θ_1 and the angle of observation is θ_2. A well-known classical relationship:

$$G(x_0) = \frac{\delta(x_0)}{\tan\theta_1 + \tan\theta_2} \tag{1}$$

can be used to approximate the height of the surface at a point x_0 by measuring the observable shift of the projected image $\delta(x_0)$ (Figure 1).

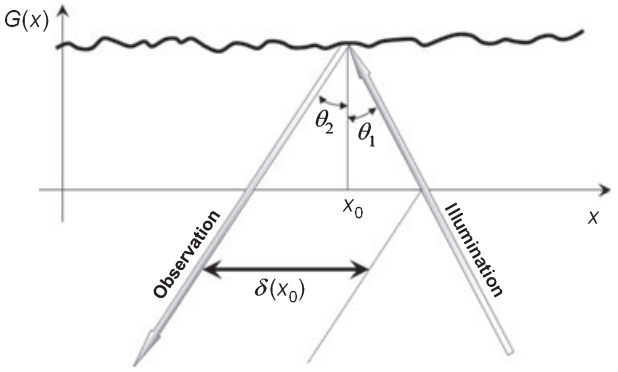

Figure 1: The observable shift of the projected image in the paraxial approximation; $G(x)$ is a deformed surface; θ_1 and θ_2 are angles of illumination and observation; $\delta(x_0)$ is the observable shift

Projection moiré is a complex optical technique, especially when an inverse problem of fringes interpretation is considered. It requires a system analysis approach. One has to consider the following basic topics: (i) camera model, (ii) projector model, (iii) reference surface and (iv) surface under analysis.

We use a paraxial model (this condition can be approximated by using a slide projector that is placed far from the specimen and by placing the imaging system far away from the specimen). In other words, we do not use a model of the camera and of the projector; the moiré grating lines are lines of equal depth with respect to a reference plane. The standard model for both the camera and the projector would be the pinhole camera with the necessary corrections to take into account the presence of a lens system. Then, one should introduce corrections to transform the observed fringes into fringes of equal depth [21–23].

Another important factor, which must be considered in practical applications, is the problem of depth of focus. A camera can focus one plane only; all the other points in the surface under analysis experience a change of coordinates that introduces an error. As we use the paraxial model, we do not need to deal with the problem of depth of focus. Otherwise, one should take care of this problem as reported in [22, 24].

We have two motives to ignore the standard model and to use a paraxial model. The first one is to show that Equation (1) is not exact even if the paraxial model is used. The second one is to explore time-averaged projection moiré effects. As mentioned previously, some recent papers use naïve considerations for the description of interference effects taking place in time-averaged images produced by projection moiré. Our objective was to derive exact relationships for time-averaged projection moiré at least for the paraxial model. The standard model could be the next step of analysis.

doi: 10.1111/j.1475-1305.2009.00625.x

First of all, we limit our study by the assumption that the direction of observation is perpendicular to the x-axis. Nevertheless, we will not loose the generality of formulations. From the geometrical point of view, the definition of two angles θ_1 and θ_2 is redundant. The frame $x0G$ can be rotated to make the x-axis perpendicular to the direction of observation; then the angle of observation becomes $\theta = \theta_1 + \theta_2$. It is clear that the function of the deformed surface will be defined is a new-rotated frame then. One would need to use a linear operator of rotation to return to the original frame $x0G$. Anyway, from now on we use only one angle. We assume that the direction of observation is perpendicular to the x-axis and the angle between the direction of illumination and the direction of observation is θ.

The basic simplification associated to the observable shift of the projected image is illustrated in Figure 2. The observable shift of the projected image on the deformed surface is $\delta(x_0)$ (if the surface coincides with the x-axis in the state of equilibrium). But a simplification that the surface is a slowly varying function (or just an error in the problem formulation) leads to a conclusion that the ordinate of the intersection point between a ray of the projected light crossing a point x_0 on the x-axis and the deformed surface equals to the $G(x_0)$ (Figure 2). In fact, this is a zero-order approximation. The observable shift would be then $\delta_0(x_0)$, and:

$$G(x_0) = \frac{\delta_0(x_0)}{\tan\theta} \tag{2}$$

Equation (2) [also Equation (1)] builds ground for a convenient experimental technique for the identification on the unknown deformed surface $G(x)$. One just needs to project a regular moiré grating on a deformed surface. It is enough to measure shifts of each grating line to approximate the shape of the surface. Almost all cited references in this paper are based on this principle. We show that in general it is not correct.

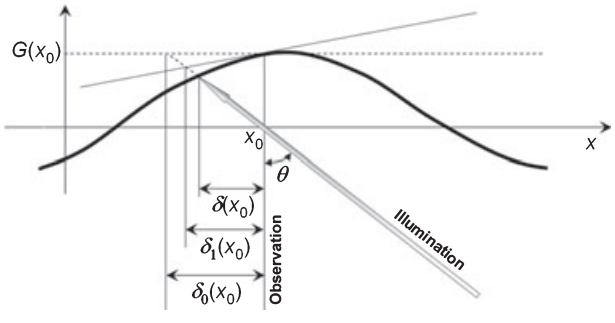

Figure 2: A geometrical representation of the projection process

Unfortunately, $\delta_0(x_0)$ is not an accurate estimate of the observable shift. A first-order approximation can produce a more accurate result (the inclined solid line in Figure 2 is a tangent to the surface at the point x_0):

$$G(x_0) + \delta_1(x_0)\frac{\mathrm{d}G(x_0)}{\mathrm{d}x} = \frac{\delta_1(x_0)}{\tan\theta} \tag{3}$$

Clearly, a derivative of the surface is involved in Equation (3). The computation of the shape of the surface becomes much more complex compared with Equation (2).

Even a higher degree of accuracy can be achieved by using higher orders of approximation (involving also higher orders of derivatives). But the object of this paper was not to present some sort of approximation. We are interested only in an exact relationship between the observable shift $\delta(x_0)$ and the height of the surface $G(x_0)$.

2.1. Exact mathematical representation of the projected image

The geometrical scheme in Figure 2 can be represented in an alternative representation in Figure 3. The projected image $F(y)$ is defined in a frame $y0F$ which is rotated in respect of the frame $x0G$ by an angle θ. The function $F(y)$ determines a greyscale level of a white light ray travelling through a point y_0 along the F-axis. Therefore, we assume that $0 \le F(y) \le 1$, where 0 represents the black color; 1 – the white color, and all intermediate values stand

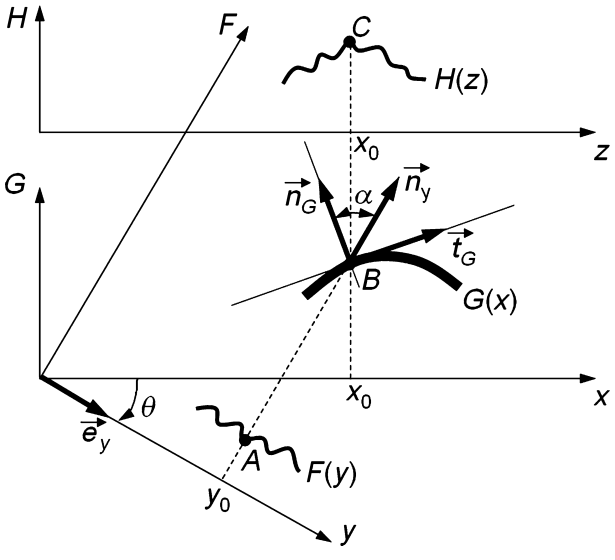

Figure 3: One-dimensional geometrical representation of the optical projection on a diffuse surface; $F(y)$ is the projected image; $G(x)$ is a diffuse deformed surface; and $H(z)$ is the observed image

doi: 10.1111/j.1475-1305.2009.00625.x

for appropriate greyscale levels. An alternative way to illustrate the function $F(y)$ in Figure 3 could be plotting a transparent film on the y-axis with a paraxial white light source on the other side of the film. Anyway, we keep the functional illustration of $F(y)$ in Figure 3 because it makes the construction of geometrical relationships easier.

As mentioned previously, we use paraxial approximation. Our motive is quite simple – first we need to derive exact relationships for a more simple case. Perspective effects caused by a point light source or by the camera lens can be examined later.

The angle of illumination θ is bounded in the interval $-\pi/2 < \theta < \pi/2$ (a negative angle θ is shown in Figure 3). The angle of observation is equal to 0; therefore, the x-axis and the z-axis are parallel. Coordinates of the marked points are: $A(y_0;\ F(y_0))$; $B(x_0;\ G(x_0))$; $C(x_0;\ H(x_0))$ (Figure 3). We introduce following vectors: $\overrightarrow{e_y}$ – unitary vector of the y-axis; $\overrightarrow{n_y}$ – unitary vector of the F-axis; $\overrightarrow{t_G}$ – tangent vector to the surface G at the point B; $\overrightarrow{n_G}$ – normal vector to the surface G at the point B. All these vectors are unitary, thus $|\overrightarrow{e_y}| = |\overrightarrow{n_y}| = |\overrightarrow{t_G}| = |\overrightarrow{n_G}| = 1$. Also, $|\overrightarrow{n_G}| \perp |\overrightarrow{t_G}|$; $|\overrightarrow{n_y}| \perp |\overrightarrow{e_y}|$. Coordinates of these vectors in the $x0G$ frame are:

$$\begin{aligned}
\overrightarrow{e_y} &= (\cos\theta; \sin\theta)\\
\overrightarrow{n_y} &= (-\sin\theta; \cos\theta)\\
\overrightarrow{t_G} &= \left(\frac{1}{\sqrt{1+\left(G'_x(x)\right)^2}}; \frac{G'_x(x)}{\sqrt{1+\left(G'_x(x)\right)^2}}\right)\\
\overrightarrow{n_G} &= \left(-\frac{G'_x(x)}{\sqrt{1+\left(G'_x(x)\right)^2}}; \frac{1}{\sqrt{1+\left(G'_x(x)\right)^2}}\right)
\end{aligned} \tag{4}$$

As mentioned previously, the surface $G(x)$ is a diffuse surface. Therefore, the observed greyscale level at a point z is:

$$H(z) = H(x) \coloneqq F(y)\cos\alpha \tag{5}$$

where

$$\cos\alpha = \left(\overrightarrow{n_y} \cdot \overrightarrow{n_G}\right) = \frac{\cos\theta + G'_x(x)\sin\theta}{\sqrt{1+\left(G'_x(x)\right)^2}} \tag{6}$$

The scalar product in Equation (6) cannot be negative because $-\pi/2 < \theta < \pi/2$ and the vector $\overrightarrow{n_G}$ cannot point downwards (the function $G(x)$ is a single-valued function).

It is clear that Equation (5) is implicit. An explicit form can be produced exploiting the relationship between coordinates of the point $B(x, G(x))$ in frames $x0G$ and $y0F$. The following equality holds for all positive x and y:

$$y = x\cos\theta - G(x)\sin\theta \tag{7}$$

Thus, finally:

$$H(x) = F(x\cos\theta - G(x)\sin\theta)\frac{\cos\theta + G'_x(x)\sin\theta}{\sqrt{1+\left(G'_x(x)\right)^2}} \tag{8}$$

The argument of the function $F(y)$ can be rewritten:

$$x\cos\theta - G(x)\sin\theta = (x - G(x)\tan\theta)\cos\theta \tag{9}$$

Equation (8) gives an exact description of the image formation process. The observable local shift equals to $G(x)\tan\theta$; the observed image is expanded by a scale $1/\cos\theta$ and the dimming (or brightening) of the observed image is described by the term:

$$\frac{\cos\theta + G'_x(x)\sin\theta}{\sqrt{1+\left(G'_x(x)\right)^2}}$$

One should not mix the local observable shift $G(x)\tan\theta$ with the zero-th order approximation $G(x_0)\tan\theta$ in Equation (2). The essential difference is that Equation (8) describes optical effects taking place at the intersection point between the ray of illumination and the deformed surface, while Equation (2) approximates the observable shift at the point of intersection between the ray of illumination and the x-axis.

Optical effects caused by the gradient of the surface to projection moiré images are analysed in [25]; corrections of the gradient effect are quantified and compared with the effect of depth of focus, this last component being more important that the gradient effect. As the function that provides the surface is an implicit function, an iterative solution is employed to obtain the final results [25]. As noted previously, we do not consider the effect of depth of focus. But our approach produces an exact result (valid only for the paraxial model) and it does not require an iterative approximation. Unfortunately, Equation (5) is an implicit equation. The derived explicit Equation (7) involves a shifted coordinate; one needs to make a coordinate change before computing the final result. That coordinate change does not depend on the gradient; the gradient is responsible only for dimming (or brightening) of the observed dynamically shifted image.

doi: 10.1111/j.1475-1305.2009.00625.x

2.2. Shadows

The formation of shadows is illustrated in Figure 4; grey-shaded areas (and thick black lines on the *z*-axis) represent the sections of the observed image where shadows are formed. A shadow starts at points A_i; B_i; C_i and finishes at points A_i; B_{i0}; C_{i0} (Figure 4).

The necessary and sufficient condition for the formation of a shadow is $\overrightarrow{n_G} \perp \overrightarrow{n_y}$ or $\cos\alpha = 0$ [Equation (6)], which yields:

$$\cos\theta + G'_x(x_i)\sin\theta = 0 \tag{10}$$

A shadow terminates at a point $B(x_{i0};\ G(x_{i0}))$. The coordinate x_{i0} can be found from the equality:

$$G(x_{i0}) - G(x_i) = -(x_{i0} - x_i)\cot\theta \tag{11}$$

No shadows exist when $\theta = 0$ and $G(x)$ is a single-valued function. All surface points are in a shadow when $|\theta| = \pi/2$.

Finally, no shadows will exist if for all x the following inequality holds true:

$$\cos\theta + G'_x(x_i)\sin\theta > 0 \tag{12}$$

(the angle between vectors $\overrightarrow{n_y}$ and $\overrightarrow{n_G}$ is acute) or

$$\cos\theta > \left|G'_x(x_i)\sin\theta\right| \tag{13}$$

2.3. A computational example

We use a simple computational example to illustrate the difference between the exact formulation in Equation (8) and the approximate relationship in Equation (2). We project a moiré grating $F(y) = 0.5 + 0.5\cos(60y)$ onto a wavy surface described by equation $G(x) = 0.3\sin(0.5x^2)$ by an angle $\theta = -\pi/4$ (Figure 5). The correct image of the projected grating is presented in Figure 5B (as mentioned previously 0 corresponds to the black colour; 1 – to the white colour). Figure 5C shows the projected grating – if the physical relationships governing the process of projection would be described by Equation (2). Next, we plot the projected grating on the *x*-axis in Figure 5D (note that the pitch of the projected grating is not $\pi/30$ because of the effect of image expansion). We find local minimums (centre lines of the dark grating lines) in Figure 5C,D and calculate absolute shifts of the grating lines. Now, heights of the deformed surface are calculated using Equation (2). Discrete points are interpolated by a continuous line showing the shape of the estimated deformed surface in Figure 5E.

It is clear that differences between the original and the reconstructed surfaces are obvious. The reconstruction could be more or less acceptable in regions where the deformed surface is a slowly varying surface. But systematic errors become huge where the gradient of the deformed surface is larger. This is a nice computational example showing the importance of the accuracy of optical relationships.

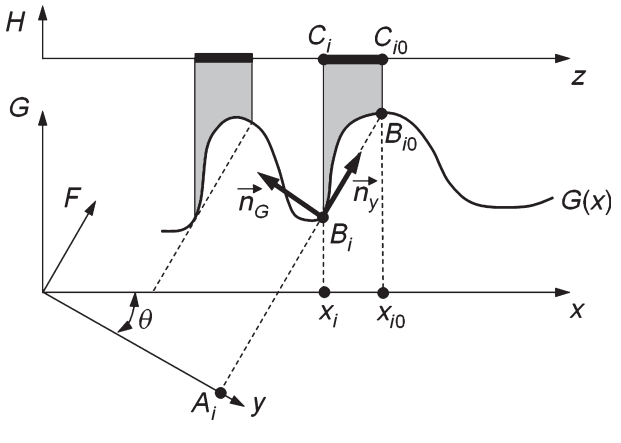

Figure 4: A schematic diagram illustrating the formation of shadows

2.4. Double-exposure projection moiré

Double-exposure projection moiré technique comprises two steps. Initially, the grating is projected obliquely to the viewing direction on a surface $G(x)$ (it can be a deformed surface) and the observed grating is photographed. Then, the specimen is deformed (the grating projection and imaging systems remain unchanged) and the observed grating is photographed again. Superposition of these two images produces moiré fringes, which can be used to identify the magnitude of the specimen's deformation.

The surface of the deformed specimen can be described as $G(x) + g(x)$, where $g(x)$ is the absolute deformation of the specimen in the direction of observation after the load was applied. We assume that the projected image is a harmonic moiré grating:

$$F(y) = \frac{1}{2} + \frac{1}{2}\cos\left(\frac{2\pi}{\lambda}y\right) \tag{14}$$

where λ is the pitch of the grating. Moreover, we will assume that the function $g(x)$ is a slowly varying function. In other words, we require that

doi: 10.1111/j.1475-1305.2009.00625.x

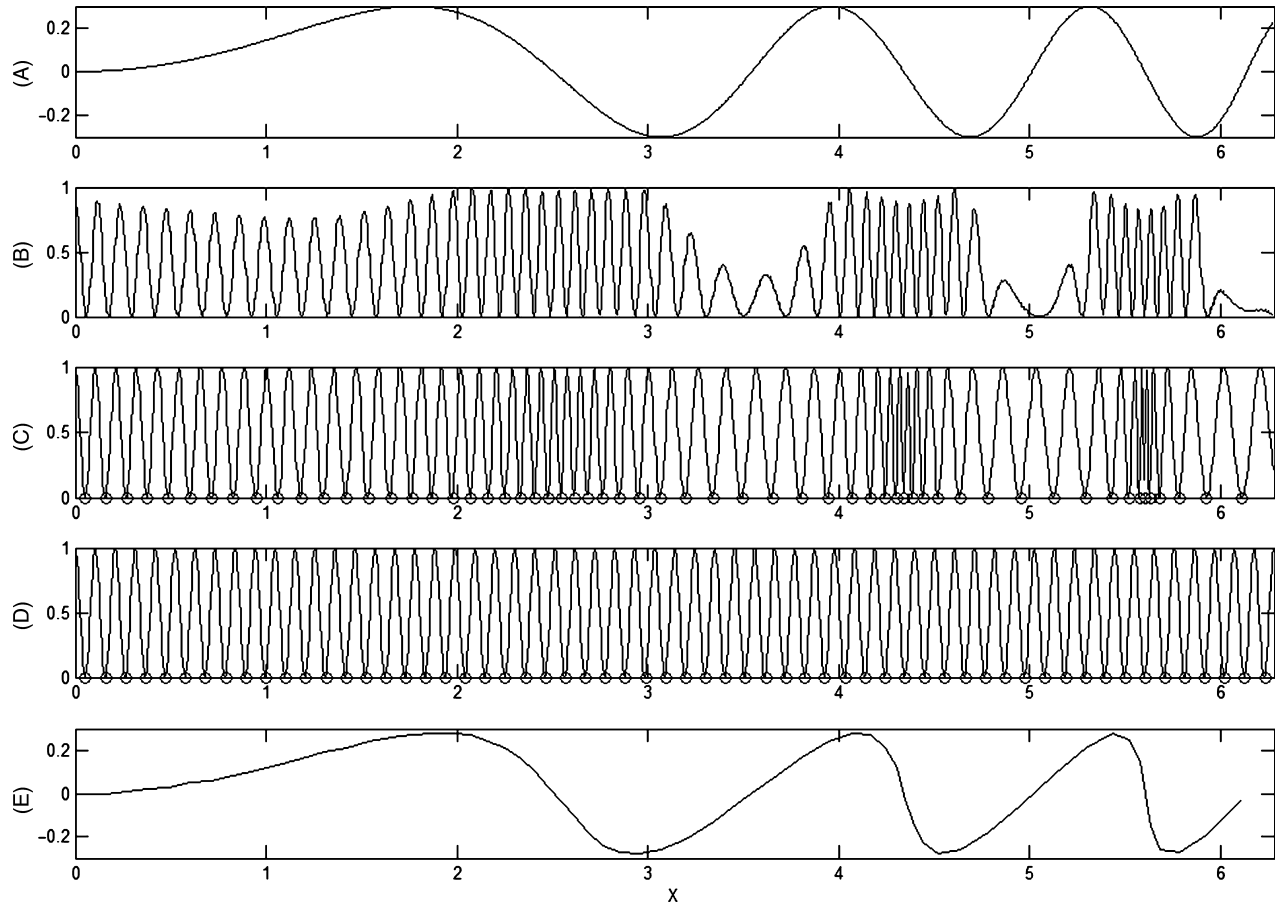

Figure 5: Computational reconstruction of the projected moiré grating: (A) a wavy surface described by equation $G(x) = 0.3\sin(0.5x^2)$; (B) correct image of the projected grating at $\theta = -\pi/4$; (C) incorrect representation of the projected grating based on Equation (1); (D) the projected grating on the x-axis; (E) the surface's reconstruction based on phase shifts calculated from (C) and (D)

$$\frac{\cos\theta + \left(G'_x(x) + g'_x(x)\right)\sin\theta}{\sqrt{1 + \left(G'_x(x) + g'_x(x)\right)^2}} \approx \frac{\cos\theta + G'_x(x)\sin\theta}{\sqrt{1 + \left(G'_x(x)\right)^2}}. \quad (15)$$

Then, additive superposition [26] of the observed grating before and after the load produces:

$$\begin{aligned}
&\frac{H_1(x) + H_2(x)}{2} \times \frac{\sqrt{1 + \left(G'_x(x)\right)^2}}{\cos\theta + G'_x(x)\sin\theta} \\
&\approx \frac{1}{2} + \frac{1}{4}\left(\cos\frac{2\pi}{\lambda}(x\cos\theta - G(x)\sin\theta)\right. \\
&\left. + \cos\frac{2\pi}{\lambda}(x\cos\theta - (G(x) + g(x)\sin\theta)\right) \\
&= \frac{1}{2} + \frac{1}{4}\cos\left[\frac{2\pi}{\lambda}\left(x\cos\theta - G(x)\sin\theta - \frac{g(x)\sin\theta}{2}\right)\right] \\
&\times \cos\left(\frac{2\pi}{\lambda}\frac{g(x)\sin\theta}{2}\right), \quad (16)
\end{aligned}$$

where $H_1(x)$ and $H_2(x)$ are observed gratings before and after the load. Equation (16) represents the effect of beats; the envelope function is

$$\frac{1}{2} \pm \frac{1}{4}\cos\left(\frac{2\pi}{\lambda}\frac{g(x)\sin\theta}{2}\right).$$

Moiré fringes will form at

$$\frac{\pi g(x)\sin\theta}{\lambda} = \frac{\pi}{2} + \pi N; \quad N = 0, \pm 1, \pm 2, \ldots \quad (17)$$

Finally, the displacement $g(x)$ in terms of fringe order N reads:

$$g(x) = \frac{(0.5 + N)\lambda}{\sin\theta} \quad (18)$$

Equation (18) is similar to a well-known relationship among the axial displacement, the pitch of the grating and the angle of illumination [15]. Nevertheless, one must remember our assumption that $g(x)$ is a slowly varying function. We can easily construct a similar figure to Figure 5 and show that the relationship in Equation (18) does not hold when gradients of $g(x)$ are high. Anyway, the main object of this paper was time-averaged projection moiré, so

doi: 10.1111/j.1475-1305.2009.00625.x

we do not concentrate more on metrological aspects of double exposure projection moiré.

3. Time-Averaged Projection Moiré

The object of this paper was to investigate the formation of time-averaged projection moiré fringes when the specimen's surface performs harmonic oscillations. The observed time-averaged image is registered by using conventional time integration techniques when the exposure time is much longer than the period of oscillations [27]. Furthermore, we analyse only harmonic oscillations of the surface:

$$G(x,t) = G(x)\sin(\omega t + \phi) \tag{19}$$

where ω is the frequency and Φ is the phase of harmonic oscillations. Then,

$$H_F(x|\theta;G(x)) = \lim_{T\to\infty}\frac{1}{T}\int_0^T H(x,t)\mathrm{d}t = \frac{1}{\pi}\int_{-\frac{\pi}{2}}^{\frac{\pi}{2}} H(x,t)\mathrm{d}t \tag{20}$$

where H_F is the observed time-averaged image;

$$H(x,t) = F(x\cos\theta - G(x)\sin\theta\cdot\sin t) \times \frac{\cos\theta + G'_x(x)\sin\theta\cdot\sin t}{\sqrt{1+\left(G'_x(x)\sin t\right)^2}} \tag{21}$$

We illustrate few properties of the time-averaging operator:

1 Let $F(y)\equiv 0$. Then $H_F(x|\theta;G(x))\equiv 0$. Time-averaged image is black if no light is projected on the surface.
2 Let $F(y)\equiv p$; p is a constant; $0\le p\le 1$. Then

$$H_F(x|\theta;G(x)) = \frac{p}{\pi}\int_{-\frac{\pi}{2}}^{\frac{\pi}{2}}\frac{\cos\theta + G'_x(x)\sin\theta\cdot\sin t}{\sqrt{1+\left(G'_x(x)\sin t\right)^2}}\,\mathrm{d}t$$

3 Let $G(x)\equiv 0$. Then $H_F(x|\theta;0) = F(x\cos\theta)\cos\theta$. Time-averaged image is similar to the projected image if the surface is flat and stationary. No time-averaged fringes are formed. If $\theta = 0$ simultaneously, $H_F(x|0;0) = F(x)$.
4 Let θ = 0. Then

$$H_F(x|0;G(x)) = \frac{F(x)}{\pi}\int_{-\frac{\pi}{2}}^{\frac{\pi}{2}}\frac{1}{\sqrt{1+\left(G'_x(x)\sin t\right)^2}}\,\mathrm{d}t$$

Time-average image and the projected image are similar if the projection angle θ = 0.

We analyse several particular cases separately.

3.1. Let $G(x) \equiv a$; a is a constant (a flat non-deformable surface oscillates up and down)

Then

$$H_F(x|\theta;a) = \frac{\cos\theta}{\pi}\int_{-\frac{\pi}{2}}^{\frac{\pi}{2}} F(x\cos\theta + a\sin\theta\cdot\sin t)\mathrm{d}t$$

We illustrate the process of time-averaging assuming that the projected image is a harmonic function defined by Equation (14):

$$H_F(x|\theta;a) = \frac{\cos\theta}{2} + \frac{\cos\theta}{2\pi}\int_{-\frac{\pi}{2}}^{\frac{\pi}{2}}\cos\left(\frac{2\pi}{\lambda}(x\cos\theta - a\sin\theta\cdot\sin t)\right)\mathrm{d}t$$
$$= \frac{\cos\theta}{2} + \frac{\cos\theta}{2}\left(\cos\frac{2\pi x\cos\theta}{\lambda}\frac{1}{\pi}\int_{-\frac{\pi}{2}}^{\frac{\pi}{2}}\cos\left(\frac{2\pi a\sin\theta}{\lambda}\sin t\right)\mathrm{d}t + \sin\frac{2\pi x\cos\theta}{\lambda}\frac{1}{\pi}\int_{-\frac{\pi}{2}}^{\frac{\pi}{2}}\sin\left(\frac{2\pi a\sin\theta}{\lambda}\sin t\right)\mathrm{d}t\right) \tag{22}$$

But

$$\frac{1}{\pi}\int_{-\frac{\pi}{2}}^{\frac{\pi}{2}}\sin\left(\frac{2\pi a\sin\theta}{\lambda}\sin t\right)\mathrm{d}t = 0$$

because the integrand is an odd function and the limits of the definite integral are symmetric. Instead of eliminating the second integral in Equation (22), we change it by another term (which is also equal to zero):

doi: 10.1111/j.1475-1305.2009.00625.x

$$\begin{aligned} H_F(x|\theta;a) &= \frac{\cos\theta}{2}+\frac{\cos\theta}{2}\cos\frac{2\pi x\cos\theta}{\lambda}\frac{1}{\pi}\left(\int_{-\frac{\pi}{2}}^{\frac{\pi}{2}}\cos\left(\frac{2\pi a\sin\theta}{\lambda}\sin t\right)\mathrm{d}t+j\int_{-\frac{\pi}{2}}^{\frac{\pi}{2}}\sin\left(\frac{2\pi a\sin\theta}{\lambda}\sin t\right)\mathrm{d}t\right)\\ &= \frac{\cos\theta}{2}+\frac{\cos\theta}{2}\cos\frac{2\pi x\cos\theta}{\lambda}\frac{1}{\pi}\left(\int_{-\frac{\pi}{2}}^{\frac{\pi}{2}}\exp\left(j\frac{2\pi a\sin\theta}{\lambda}\sin t\right)\mathrm{d}t\right)\\ &= \frac{\cos\theta}{2}+\frac{\cos\theta}{2}\cos\frac{2\pi x\cos\theta}{\lambda}\lim_{T\to\infty}\left(\frac{1}{T}\int_0^T\exp\left(j\frac{2\pi a\sin\theta}{\lambda}\sin t\right)\mathrm{d}t\right)\\ &= \frac{\cos\theta}{2}+\frac{\cos\theta}{2}\cos\frac{2\pi x\cos\theta}{\lambda}J_0\left(\frac{2\pi a\sin\theta}{\lambda}\right), \end{aligned} \tag{23}$$

where $j^2 = -1$ and J_0 is zero-order Bessel function of the first kind [28];

$$J_0(x)=\lim_{T\to\infty}\frac{1}{T}\int_0^T\exp(jx\sin t)\mathrm{d}t$$

We show that properties C and D hold before continuing the discussion on time-averaging effects. Since $J_0(0) = 1$,

$$H_F(x|\theta;0)=\cos\theta\left(\frac{1}{2}+\frac{1}{2}\cos\frac{2\pi x\cos\theta}{\lambda}\right)=F(x\cos\theta)\cos\theta \tag{24}$$

On the other hand,

$$H_F(x|0;a)=\frac{1}{2}+\frac{1}{2}\cos\frac{2\pi x}{\lambda}=F(x) \tag{25}$$

Such time-averaging reminds classical in-plane time-averaged geometric moiré, when an array of parallel lines (moiré grating) is printed on a surface of a non-deformable body and it performs in-plane oscillations in the direction orthogonal to the constitutive grating lines. If greyscale variation on the surface of a one-dimensional non-deformable body is

$$\frac{1}{2}+\frac{1}{2}\cos\left(\frac{2\pi}{\lambda}x\right)$$

and the amplitude of harmonic oscillation is a, time-averaged greyscale level reads:

$$\frac{1}{2}+\frac{1}{2}\cos\frac{2\pi x}{\lambda}J_0\left(\frac{2\pi a}{\lambda}\right)$$

The envelope function which modulates the original moiré grating can be expressed as:

$$\frac{1}{2}\pm\frac{1}{2}J_0\left(\frac{2\pi a}{\lambda}\right)$$

The effect of beats could be observed if the amplitude of oscillation would be varied continuously. Time-averaged image will become blurred at such values of a where $2\pi a/\lambda = r_i$; $i = 1, 2, \ldots$, where r_i is the i-th root of the zero-order Bessel function of the first kind.

Time-averaged projection moiré images will also get blurred at certain amplitudes of oscillations. The difference from time-average geometric moiré is that these amplitudes are $a_i = r_i(\lambda/2\pi\sin\theta)$; $i = 1, 2, \ldots$; $\theta \neq 0$ (at $\theta = 0$ the property 4 holds true). Another difference is that the greyscale level of the blurred image is $\cos\theta/2$ instead of 0.5 (time-averaged projection moiré image is darker than time-averaged geometric moiré image). Otherwise, the properties of both time-averaging processes are similar.

3.2. Let $G(x) = ax$; a is a constant (the flat non-deformable surface performs angular oscillations around a pivot point at $x = 0$)

Initially, we assume that $\theta = 0$. Then,

$$H_F(x|0;ax)=\frac{F(x)}{\pi}\int_{-\frac{\pi}{2}}^{\frac{\pi}{2}}\frac{1}{\sqrt{1+(a\sin t)^2}}\,\mathrm{d}t \tag{26}$$

Recall that the observation angle is also equal to 0. Thus, the observed image will not be deformed at any instantaneous moment of the oscillation. Consequently, no time-averaged fringes will be formed in the observed image. The only effect caused by the oscillation is the darkening of the observed image (the higher is the amplitude a, the darker is the time-averaged image).

If $\theta \neq 0$, then

$$\begin{aligned} H_F(x|\theta;ax) = \frac{1}{\pi}\int_{-\frac{\pi}{2}}^{\frac{\pi}{2}}&F(x\cos\theta-ax\sin\theta\cdot\sin t)\\ &\times\frac{\cos\theta+a\sin\theta\cdot\sin t}{\sqrt{1+(a\sin t)^2}}\,\mathrm{d}t \end{aligned} \tag{27}$$

Instantaneous observed images at time moments of extreme deflections take the following form:

doi: 10.1111/j.1475-1305.2009.00625.x

$$H\left(x,-\frac{\pi}{2}\right)=F((\cos\theta+a\sin\theta)x)\frac{\cos\theta-a\sin\theta}{\sqrt{1+a^2}};$$
$$H\left(x,\frac{\pi}{2}\right)=F((\cos\theta-a\sin\theta)x)\frac{\cos\theta+a\sin\theta}{\sqrt{1+a^2}} \quad (28)$$

Again, we assume that the projected image is a regular moiré grating described by Equation (14). Then, the pitch of the observed image varies during the angular oscillations of the flat surface. The pitch of the grating is $\lambda/(\cos\theta+a\sin\theta)$ at $t=-\pi/2$; λ at $t=0$ and $\lambda/(\cos\theta-a\sin\theta)$ at $t=\pi/2$.

Such oscillation of the pitch of the grating produces a complex pattern of time-averaged interference fringes. Analogous time-averaging process occurs when geometric moiré techniques are applied to register in-plane oscillations of structures with pitches varying in time. The formation of time-averaged fringes is now governed not by zero-order Bessel function of the first kind; moreover, the relationship between the fringe orders of the amplitude of oscillation becomes implicit [29]. Quantitative fringe-counting techniques are applicable only when the amplitude of oscillation is relatively small.

We illustrate the formation of time-averaged fringes in Figure 6; the oscillating surface is defined by $G(x,t)=0.02x\sin t$; the pitch of the projected harmonic grating is $\lambda=0.04$. Figure 6B–D illustrates observable images at different moments of time. Figure 6E illustrates the time-averaged observable image.

3.3. Let $G(x) = a\sin(kx+\varphi)$, where a is the amplitude of the standing wave; k is the wave number and φ is the phase

Such surface oscillations (standing waves) are common in science and engineering; therefore, it is important to understand the process of formation of time-averaged projected fringes. Naïve considerations could lead to such loose interpretations that the formation of time-averaged fringes is governed by processes described in the Section 3.1 in regions around peaks of the standing wave and by the processes described in the Section 3.2 in regions around nodes of the standing wave.

Time-averaged fringes can be approximated analytically if $G(x)$ is a slowly varying function. In that case, one may assume that

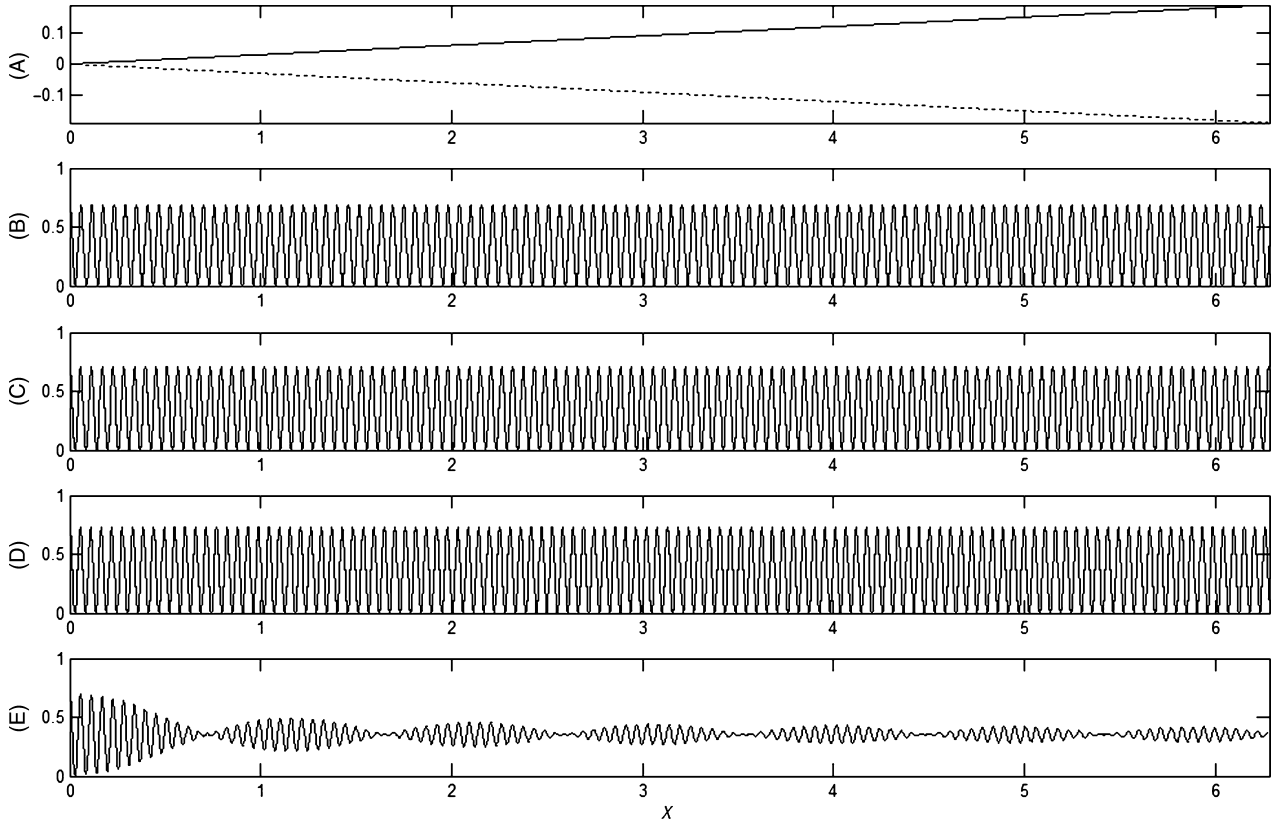

Figure 6: The formation of time-averaged projection fringes on a flat surface oscillating around a pivot point; $F(y)=0.5+0.5\cos(2\pi y/0.04)$; $G(x,t)=0.02x\sin t$; $\theta=\pi/4$; (A) the oscillating surface (the solid and the dotted lines show maximum deflections of the surface); (B) instantaneous observed image at $t=\pi/2$; (C) at $t=\pi$ and (D) at $t=3\pi/2$; (E) time-averaged image

doi: 10.1111/j.1475-1305.2009.00625.x

$$\frac{\cos\theta + G'_x(x)\sin\theta\cdot\sin t}{\sqrt{1+\left(G'_x(x)\sin t\right)^2}} \approx \cos\theta \tag{29}$$

When the projected grating is a harmonic moiré grating defined by Equation (14),

$$G(x) = \lambda r_i/(2\pi\sin\theta), \tag{31}$$

where i is the order of the time-averaged fringe and r_i is the i-th root of the zero-order Bessel function of the first type.

$$\begin{aligned} H_F(x|\theta;G(x)) &= \lim_{T\to\infty}\frac{1}{T}\int_0^T H(x,t)\mathrm{d}t \approx \cos\theta\lim_{T\to\infty}\frac{1}{T}\int_0^T\left(\frac{1}{2}+\frac{1}{2}\cos\left(\frac{2\pi}{\lambda}(x\cos\theta - G(x)\sin\theta\cdot\sin t)\right)\right)\mathrm{d}t \\ &= \frac{\cos\theta}{2}+\frac{\cos\theta}{2}\lim_{T\to\infty}\frac{1}{T}\int_0^T\cos\left(\frac{2\pi}{\lambda}x\cos\theta\right)\cos\left(\frac{2\pi}{\lambda}G(x)\sin\theta\cdot\sin t\right)\mathrm{d}t \\ &= \frac{\cos\theta}{2}+\frac{\cos\theta}{2}\cos\left(\frac{2\pi}{\lambda}x\cos\theta\right)J_0\left(\frac{2\pi}{\lambda}G(x)\sin\theta\right) \end{aligned} \tag{30}$$

The envelope function determining the formation of fringes is

$$\frac{\cos\theta}{2}\pm\frac{\cos\theta}{2}J_0\left(\frac{2\pi}{\lambda}G(x)\sin\theta\right)$$

The relationship among the amplitude of the standing wave, the pitch of the projected grating and the order of a time-averaged fringe is then:

We illustrate the formation of time-averaged fringes in Figure 7; the oscillating surface is defined by $G(x,t) = 0.1\sin x\sin t$; the pitch of the projected harmonic grating is $\lambda = 0.04$. Figure 6B–D illustrates observable images at different moments of time. Figure 6E illustrates the time-averaged observable image. The observable grating is sharpest in regions where the amplitude of the standing wave is smallest (at nodal points of the standing wave) because

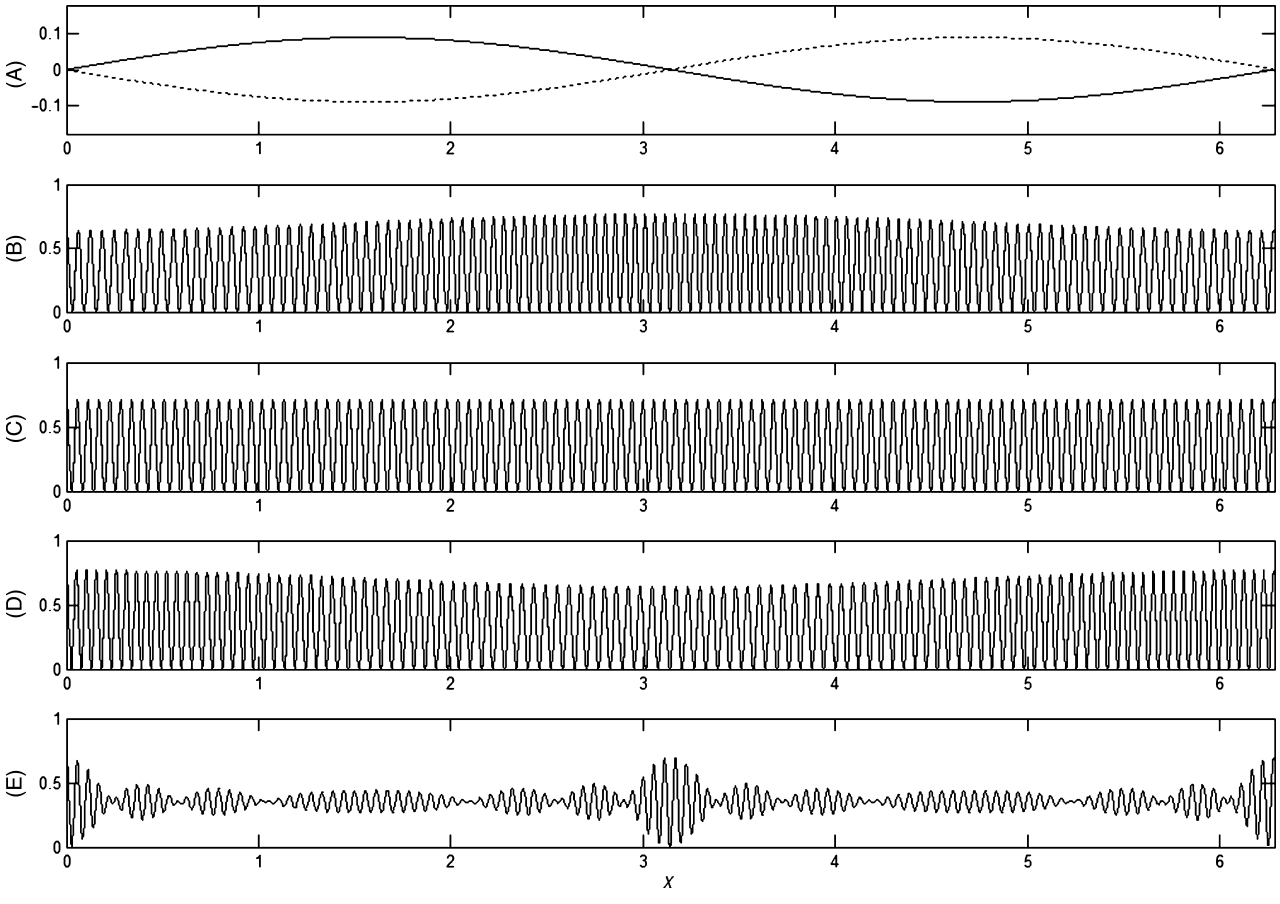

Figure 7: The formation of time-averaged projection fringes on a surface of a standing wave; $F(y) = 0.5 + 0.5\cos(2\pi y/0.04)$; $G(x,t) = 0.1\sin x\sin t$; $\theta = \pi/4$; (A) the oscillating surface (the solid and the dotted lines show maximum deflections of the surface); (B) instantaneous observed image at $t = \pi/2$; (C) at $t = \pi$ and (D) at $t = 3\pi/2$; (E) time-averaged image

doi: 10.1111/j.1475-1305.2009.00625.x

$J_0(0) = 1$. The observable grating gets blurred as the amplitude of the standing wave gets higher. This decay of sharpness of the time-averaged image is not monotonic; it is governed by the envelope function described above. Only three time-averaged fringes are developed in Figure 7E. And again one must keep in mind that approximation in Equation (30) is acceptable only when $G(x)$ is a slowly varying function.

Although time-averaged geometrical moiré fringes were introduced in 1979 [30], interpretation of time-averaged projection moiré fringes is a much more complex problem. As mentioned previously, these problems are still investigated 25 years later [19, 20]. Our approach is clear – we use a simple paraxial model and try to derive exact relationships.

4. Analogies and Discussion

Equation (21) can be rewritten in the form:

$$H_F(x|\theta; G(x)) = \frac{\cos\theta}{\pi}\int_{-\frac{\pi}{2}}^{\frac{\pi}{2}} F(\cos\theta\cdot(x + G(x)\tan\theta\sin t))\frac{1 + (G'_x(x)\tan\theta)\sin t}{\sqrt{1 + (G'_x(x)\sin t)^2}}\mathrm{d}t \tag{32}$$

Introduction of a new function $\hat{F}(z) = F(z\cos\theta)$ and a new variable $u = (G(x)\tan\theta)\sin t$ transforms Equation (32) to the following form:

$$H_F(x|\theta; G(x)) = \frac{\cos\theta}{\pi}\int_{-G(x)\tan\theta}^{G(x)\tan\theta} \hat{F}(x+u)\frac{1 + \frac{G'_x(x)}{G(x)}u}{\sqrt{1 + \left(\frac{G'_x(x)}{G(x)}\right)^2\frac{u^2}{\tan^2\theta}}}\frac{\mathrm{d}u}{\sqrt{(G(x)\tan\theta)^2 - u^2}} \tag{33}$$

We introduce the following function:

$$\rho(u|\theta, G(x)) = \frac{1 + \frac{G'_x(x)}{G(x)}u}{\sqrt{1 + \left(\frac{G'_x(x)}{G(x)}\right)^2\frac{u^2}{\tan^2\theta}}} = \frac{(G(x) + G'_x(x)u)\tan\theta}{\sqrt{G^2(x)\tan^2\theta + G'^2_x(x)u^2}} \tag{34}$$

Then, Equation (33) yields:

$$H_F(x|\theta; G(x)) = \frac{\cos\theta}{\pi}\int_{-s}^{s}\hat{F}(x+u)\rho(u|\theta, G(x))\frac{\mathrm{d}u}{\sqrt{s^2 - u^2}}, \tag{35}$$

where $s = G(x)\tan\theta$.

The function $\rho(u|\theta, G(x))$ can be considered as a measure determining the dynamical complexity of the surface $G(x)$. Really, $\rho(u|\theta, G(x)) = 1$ if $G(x) = a$. Then,

$$H_F(x|\theta; a) = \frac{\cos\theta}{\pi}\int_{-s}^{s}\hat{F}(x+u)\frac{\mathrm{d}u}{\sqrt{s^2 - u^2}} \tag{36}$$

This is another, operator form [31] of representation of interference effects described in the Section 3.1.

It can be noted that we have not used Fourier methods for analysis of moiré effects so far. Fourier method is almost a standard analysis technique for in-plane geometric moiré [Patorski], although it is also applied for out-of plane moiré [32]. Nevertheless, we did not exploit Fourier techniques. The main reason for doing that is because analytical Fourier techniques employ the truncation of infinite series and concentrate on the first terms only. Thus, unavoidable approximation errors are introduced. Although Fourier methods can help to understand physical processes (especially double exposure effects) directly, our goal was to derive exact relationships (for the paraxial model).

5. Two-Dimensional Example

In general, the image plane, the surface plane and the observation plane can be located independently in the three-dimensional space. As we assume that the angle of observation is zero, the *H*-plane and the *G*-plane are parallel (Figure 8). The angle of illumination is θ; thus we assume (without loss of generality) that the angle between the *F*-plane and the *G*-plane planes is also θ (Figure 8). As previously, the function $F(y, v)$ determines greyscale levels of the projected image; $G(x, v)$ – the shape of the surface and $H(x, v)$ – greyscale levels of the observed image. Then,

doi: 10.1111/j.1475-1305.2009.00625.x

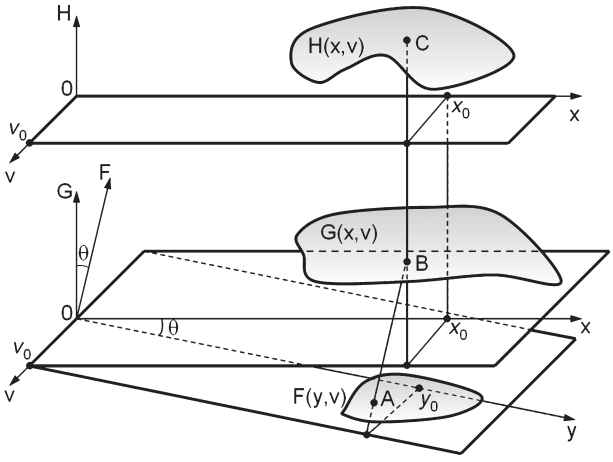

Figure 8: A schematic representation of the projection process

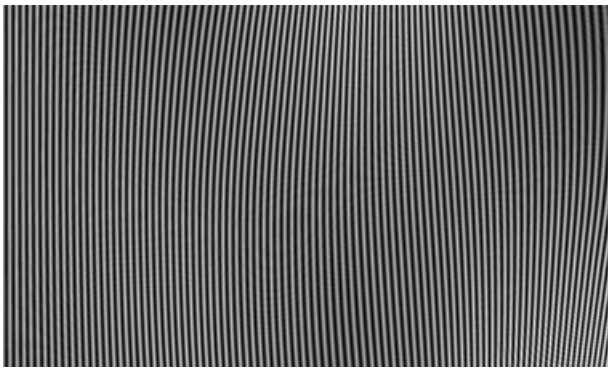

Figure 10: Instantaneous observable grating at the moment of maximum deflections from the state of equilibrium

$$H_F(x,v|\theta,G(x,v)) = \lim_{T\to\infty}\frac{1}{T}\int_0^T F(x\cos\theta + G(x,v)\sin\theta\cdot\sin t;v)\frac{\cos\theta+\sin\theta\cdot\sin t\cdot\partial G(x,v)/\partial x}{\sqrt{1+(\sin t\cdot\partial G(x,v)/\partial x)^2}}\mathrm{d}t \tag{37}$$

Coordinates of marked points in appropriate frames (Figure 8) are: $A(y_0,v_0,F(y_0,v_0))$; $B(x_0,v_0,G(x_0,v_0))$; and $C(x_0,v_0,H(y_0,v_0))$.

We use a model of a vibrating cantilever to illustrate the process of the formation of time-averaged projection fringes. Figure 9 shows maximum deflections from the state of equilibrium in the process of harmonic oscillations calculated by finite element method. The contour map at the bottom illustrates the field of amplitudes in a two-dimensional projection. The cantilevered plate oscillates up and down along the vertical axis; it does not expand or shrink along other axes.

A harmonic moiré grating $F(x,y) = 0.5 + 0.5\cos(50x)$ is projected on the surface of the cantilever; the angle of projection is $\theta = \pi/4$. The observable grating at the moment of maximum deflections from the state of equilibrium is shown in Figure 10. Figure 11 also shows the observable grating at the moment of maximum deflections but a half of the period of oscillations. Finally, Figure 12 shows the time-averaged observable image. Time-averaged moiré fringes are clearly visible there. The field of maximum deflections from the state of equilibrium can be considered as a slowly varying function; maximum amplitude of oscillation is around 0.15 while the longitudinal dimension of the cantilever is over 6 (Figure 9). Therefore, the relationship among the order of a time-averaged fringe in Figure 12, the amplitude of the standing wave and the pitch of the projected grating can be approximated by Equation (31). In other words, the pattern of time-averaged

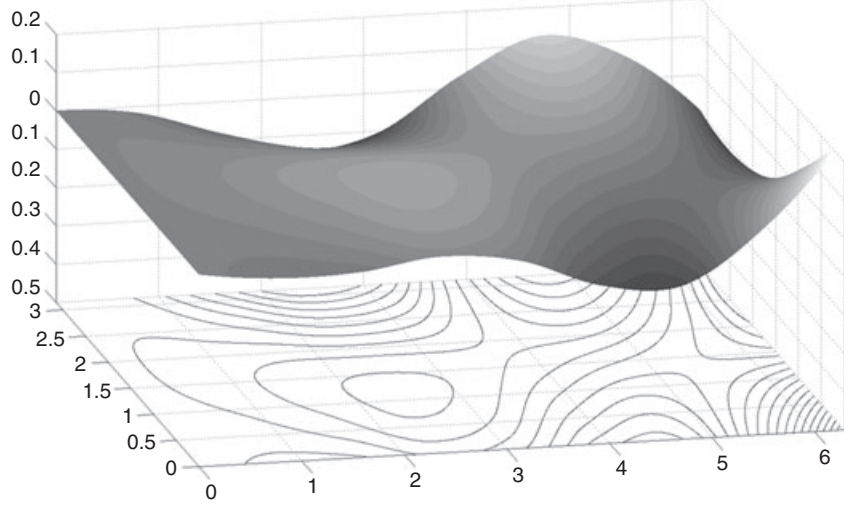

Figure 9: A numerical model of the vibrating cantilevered plate; the shape of the cantilever and the contour map of the field of amplitudes are shown at the moment of maximum deflections from the state of equilibrium

doi: 10.1111/j.1475-1305.2009.00625.x

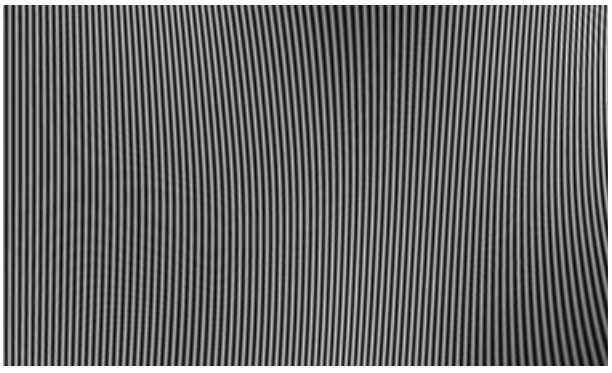

Figure 11: Instantaneous observable grating at the moment of opposite maximum deflections from the state of equilibrium

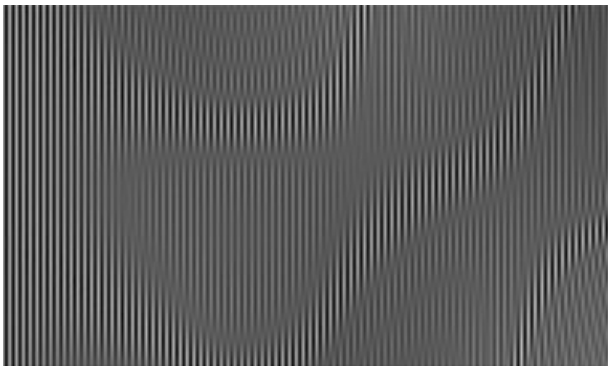

Figure 12: The observable pattern of time-averaged fringes

fringes in Figure 12 can be considered as isolines of the field of amplitudes.

It must be noted that we analyse only one moiré projection. More than one projector must be introduced if one wants to get complete information on the surface's geometry [21, 24]. In general, surfaces are tensors of second order and hence one single projection does not provide enough information to achieve high accuracy [22]. Anyway, the goal of this paper was not to redesign the theory of inverse problems. The goal was to give an accurate interpretation of projection moiré fringes at a given angle of illumination in a paraxial approximation.

So far we have used an assumption that the cantilever vibrates harmonically. It is well known that non-linear systems can exhibit periodic, quasiperiodic and even chaotic responses under periodic forcing. Applicability of reflection moiré techniques for chaotic oscillations in rigorously explored in [33]; a relationship between the largest Lyapunov exponent of the chaotic process and the time-averaged greyscale intensity is derived. The effect of the disappearance of time-averaged fringes is demonstrated for a centrally clamped rotating circular disk [33]. But physical principles of the formation of fringes for reflection and projection moiré optical techniques are different. Thus, we leave a detailed analysis of chaotic processes for the future research, although numerical experiments show the same effect of the disappearance of projected moiré fringes.

6. Concluding Remarks

We have derived an exact relationship governing the formation of projection moiré fringes on a curved surface. It has been demonstrated that systematic errors done with the approximation of the observable shift of grating lines can lead to serious misinterpretations of physical processes taking place in analysed systems.

This exact analytical result (for the paraxial model) enabled us to derive more accurate approximations for time-averaging projection moiré compared with what has been done before, under the assumption that the variation of the surface is a slowly varying function. Derived explicit relationships among heights of the measured surface (in static and especially dynamic applications), the pitch of the projected grating and the order of a moiré fringe can help to better understand processes taking place whenever projection moiré techniques are used for investigation of dynamical systems, and minimise general budgets of measurement uncertainties.

REFERENCES

1. Kobayashi, A. S. (1993) *Handbook on Experimental Mechanics*, 2nd edn. SEM, Bethel.
2. Breque, C., Dupre, J. C. and Bremand, F. (2004) Calibration of a system of projection moiré for relief measuring: biomechanical applications. *Opt. Lasers Eng.* **41**, 241–260.
3. Lehmann, M., Jacquot, P. and Faccini, M. (1999) Shape measurements on large surfaces by fringe projection. *Exp. Tech.* **23**, 31–35.
4. Kimber, M. and Blotter, J. (2006) A novel technique to determine difference contours between digital and physical objects for projection moiré interferometry. *Opt. Lasers Eng.* **44**, 25–40.
5. Ryu, W. J., Kang, Y. J., Baik, S. H. and Kang, S. J. (2008) A study on the 3-D measurement by using digital projection moiré method. *Optik Int. J. Light Electron Opt.* **119**, 453–458.
6. Kim, S. W., Choi, Y. B. and Oh, J. T. (1999) Reverse engineering: high speed digitization of free-form surfaces by phase-shifting grating projection moiré topography. *Int. J. Mach. Tools Manufact.* **39**, 389–401.
7. He, Y. M., Tay, C. J. and Shang, H. M. (1998) Deformation and profile measurement using the digital projection grating method. *Opt. Lasers Eng.* **30**, 367–377.
8. Asundi, A. (1993) Computer aided moiré methods. *Opt. Lasers Eng.* **18**, 213–238.

doi: 10.1111/j.1475-1305.2009.00625.x

9. Scott, J. C. (1969) Moiré fringes for liquid surface wave measurement. *Opt. Technol.* **1**, 240–243.
10. Der Hovanesian, J. and Hung, Y. Y. (1971) Moiré contour-sum, contour-difference and vibration analysis of arbitrary objects. *Appl. Opt.* **10**, 2734–2738.
11. Harding, K. G. and Harris, J. S. (1983) Projection moiré interferometer for vibration analysis. *Appl. Opt.* **22**, 856–861.
12. Van Paepegem, W., Shulev, A., Moentjens, A., Harizanova, J., Degrieck, J. and Sainov, V. (2008) Use of projection moiré for measuring the instantaneous out-of-plane deflections of composite plates subject to bird strike. *Opt. Lasers Eng.* **46**, 527–534.
13. Wagemann, E. U., Haist, T., Schönleber, M. and Tiziani, H. J. (1999) Fast shape and position control by moiré-filtering and object-adapted fringe projection. *Opt. Commun.* **165**, 7–10.
14. Moga, P. and Cloud, G. (1991) . A study of scapular displacement by differential moire methods. *Proc. SEM Spring Conf. On Expt Mechanics*, Milwaukee, 736–750.
15. Cloud, G. (2006) Optical methods in experimental mechanics. Part 22: Projection moiré. *Exp. Tech.* **30**, 15–18.
16. Buytaert, J. A. N. and Dirckx, J. J. J. (2007) Design considerations in projection phase-shift moiré topography based on theoretical analysis of fringe formation. *J. Opt. Soc. Am. A* **24**, 2003–2013.
17. Sutton, M. A., Zhao, W., McNeill, S. R., Schreier, H. W. and Cao, Y. J. (2001) Development and assessment of a single image fringe projection method for dynamics applications. *Exp. Mech.* **41**, 205–217.
18. Cosola, E., Genovese, K., Lamberti, L. and Pappalettere, C. (2008) A general framework for identification of hyper-elastic membranes with moiré techniques and multi-point simulated annealing. *Int. J. Solids Struct.* **45**, 6074–6099.
19. Hopstone, P., Katz, A. and Politch, J. (1989) Infrastructure of time-averaged projection moiré fringes in vibration analysis. *Appl. Opt.* **28**, 5305–5311.
20. Mitchell, A. K. (2005) Optical modal analysis using white-light projected fringes. *Exp. Mech.* **45**, 250–258.
21. Schreiber, W. and Notni, G. (2000) Theory and arrangements of self-calibrating whole body three-dimensional measurement systems using fringe projection technique. *Opt. Eng.* **39**, 159–169.
22. Sciammarella, C., Lamberti, L. and Boccaccio, A. (2008) General model for moiré contouring, part 1: theory. *Opt. Eng.* **47**, Paper No. 033605.
23. Sciammarella, C., Lamberti, L., Boccaccio, A., Cosola, E. and Posa, D. (2008) General model for moiré contouring, part 2: applications. *Opt. Eng.* **47**, Paper No. 033606.
24. Ikeda, Y., Yoneyama, S., Fujigaki, M. and Morimoto, Y. (2003) Absolute phase analysis method for three-dimensional surface profilometry using frequency-modulated grating. *Opt. Eng.* **42**, 1249–1255.
25. Sciemmarella, C. A., Lamberti, L. and Sciammarella, F. M. (2005) High accuracy contouring using projection moiré. *Opt. Eng.* **44**, Paper No. 093605.
26. Patorski, K. and Kujawinska, M. (1993) *Handbook of the Moiré Fringe Technique*. Elsevier, Amsterdam.
27. Ragulskis, M. and Navickas, Z. (2007) Hash function construction based on time average moiré. *Discrete Contin. Dyn. Syst. Series B* **8**, 1007–1020.
28. Watson, G. N. (1995) *A Treatise on the Theory of Bessel Functions*. Cambridge University Press, Cambridge.
29. Ragulskis, M. and Navickas, Z. (2008) Time average geometric moiré – back to the basics. *Exp. Mech.* DOI: 10.1007/s11340-008-9167-8.
30. Liang, C. Y., Hung, Y. Y., Durelli, A. J. and Hovanesian, J. D. (1979) Time-averaged moiré method for in-plane vibration analysis. *J. Sound Vib.* **62**, 267–275.
31. Navickas, Z. and Ragulskis, M. (2007) Representation of time averaged vibrating images in the operator format. *J. Vibroengineering* **9**, 1–8.
32. Morimoto, Y., Gascoigne, H. E. and Post, D. (1994) Carrier pattern analysis of moiré interferometry using the Fourrier transform moiré method. *Opt. Eng.* **33**, 2646–2653.
33. Ragulskis, M., Sanjuan, M. A. F. and Saunoriene, L. (2007) Applicability of time-average moiré techniques for chaotic oscillations. *Phys. Rev. E* **76**, Article No. 036208.

doi: 10.1111/j.1475-1305.2009.00625.x